Neutrino emission characteristics and detection opportunities based on three-dimensional supernova simulations

Irene Tamborra,[1] Georg Raffelt,[2] Florian Hanke,[3,4] Hans-Thomas Janka,[3] and Bernhard Müller[5]

[1] *GRAPPA Institute, University of Amsterdam, Science Park 904, 1098 XH Amsterdam, The Netherlands*
[2] *Max-Planck-Institut für Physik (Werner-Heisenberg-Institut), Föhringer Ring 6, 80805 München, Germany*
[3] *Max-Planck-Institut für Astrophysik, Karl-Schwarzschild-Str. 1, 85748 Garching, Germany*
[4] *Physik Department, Technische Universität München, James-Franck-Str. 1, 85748 Garching, Germany*
[5] *Monash Center for Astrophysics, School of Mathematical Sciences, Building 28, Monash University, Victoria 3800, Australia*

(Dated: August 27, 2014)

The neutrino emission characteristics of the first full-scale three-dimensional supernova simulations with sophisticated three-flavor neutrino transport for three models with masses 11.2, 20 and 27 $M_\odot$ are evaluated in detail. All the studied progenitors show the expected hydrodynamical instabilities in the form of large-scale convective overturn. In addition, the recently identified LESA phenomenon (lepton-number emission self-sustained asymmetry) is generic for all our cases. Pronounced SASI (standing accretion-shock instability) activity appears in the 20 and 27 $M_\odot$ cases, partly in the form of a spiral mode, inducing large but direction and flavor-dependent modulations of neutrino emission. These modulations can be clearly identified in the existing IceCube and future Hyper-Kamiokande detectors, depending on distance and detector location relative to the main SASI sloshing direction.

PACS numbers: 14.60.Lm, 97.60.Bw

arXiv:1406.0006v2 [astro-ph.SR] 26 Aug 2014

I. INTRODUCTION

The neutrino signal of the next nearby core-collapse supernova (SN) will be measured in many detectors that will register tens to hundreds of events, assuming a fiducial distance in the galaxy of 10 kpc [1]. The largest statistics will be provided by Super-Kamiokande [2, 3] with roughly 10^4 and IceCube [4–6] with roughly 10^6 events, the latter without event-by-event energy information. In the context of neutrino oscillation physics, additional large detectors are in different phases of planning, notably JUNO [7], a 20 kt liquid scintillator detector, Hyper-Kamiokande [8], a megaton water Cherenkov detector, and a 30 kt liquid-argon time-projection chamber [9, 10]. The main problem, of course, is that galactic SNe are rare, perhaps one every few decades [11–20]. Clearly we should prepare well for such a once-in-a-lifetime opportunity and should understand in advance what could be learnt from such an observation.

The low-statistics neutrino signal of SN 1987A has confirmed the general picture of stellar core collapse, but was too sparse to extract much astrophysical detail [21]. On the other hand, it has provided many useful particle-physics lessons, notably on the possible energy loss in new forms of radiation such as axions [22, 23]. A future observation will refine such arguments, but the real benefit of high statistics may be detailed astrophysical information on the physics of core collapse [24–30]. Thirty years after the formulation of the neutrino-driven delayed-explosion paradigm by Bethe and Wilson [31, 32], we still can not be sure that their theory is not missing some important ingredient [33].

According to their scenario, a shock wave forms at core bounce, stalls after reaching a radius of 100–200 km, and is revived by neutrino heating after tens to hundreds of milliseconds, depending on progenitor properties and accretion rate of stellar matter that continues to collapse. Moreover, observed SN asymmetries and two-dimensional (2D) [27, 34–42] and 3D [43–51] hydrodynamical simulations imply that SN explosions are inherently multi-dimensional. During the accretion phase, large-scale convective overturn develops in the neutrino-heated postshock layer and the standing accretion shock instability (SASI) [52] can arise, involving global deformation and sloshing motions of the shock front [52–54].

In the course of the present research project we have recently discovered the LESA phenomenon ("lepton-number emission self-sustained asymmetry") [55]. The deleptonization (ν_e minus $\bar{\nu}_e$) flux during the accretion phase develops a pronounced dipole pattern, i.e. the lepton-number flux emerges predominantly in one hemisphere. We have identified a feed-back loop as the likely cause of this effect. Its elements are asymmetric accretion caused by shock-wave deformation and asymmetric neutrino heating behind the shock front causing the shock-front deformation. It is not yet clear if LESA is a benign curiosity of multi-dimensional SN physics or an important player in the overall core-collapse phenomenology, perhaps in conjunction with neutrino flavor conversion. Either way, its discovery certainly shows that in multi-dimensional SN models there is room for hitherto unsuspected new phenomena.

The various hydrodynamical instabilities appearing in 3D core collapse during the phase of a standing accretion shock imply that the neutrino signal expected from the next nearby SN can show fast modulations and depends on observer location relative to the main direction of SASI sloshing and relative to the LESA dipole direction.

The main purpose of our paper is to explore these issues based on our current portfolio of 3D core-collapse models with full-scale three-flavor neutrino transport. The progenitor masses are 11.2, 20 and 27 $M_\odot$, all of them show the LESA phenomenon and the two heavier models show pronounced SASI activity.

The present paper expands on our earlier *Physical Review Letter* [28] where we have reported the appearance of signal modulations by SASI that are detectable in IceCube and the future Hyper-Kamiokande detector. In the context of 2D models, this point had been made earlier [25]. On the other hand, it had also been shown that convective overturn alone produces signal modulations that can be detected only if the SN is very close [26]. Therefore, detectable signal modulations are typically tied to the appearance of SASI.

A vigorous debate among SN modelers had revolved around the question if SASI indeed appears in 3D models or if its growth would be suppressed by large-scale convective overturn [49, 56, 57]. Meanwhile SASI activity in 3D SN models with different neutrino treatments was found by several authors [50, 58, 59], but such a convergence of qualitative numerical conclusions, of course, leaves open the question of what actually happens in nature. The appearance of the SASI is driven by progenitor-dependent conditions, which determine the growth rates of the SASI and convective instability in the postshock accretion layer [53]. A neutrino observation of SASI modulations would be a unique smoking gun to prove its very existence in real-life core-collapse events.

When we studied more closely how the neutrino emission characteristics depend on observer direction we noticed a pronounced asymmetry in the lepton-number flux, whereas the overall neutrino luminosity is nearly spherically symmetric except for the SASI modulations [55]. A detailed study of the various elements of this puzzling LESA phenomenon, however, has yielded support for its possibly physical origin. In particular, we believe that we have identified the feedback loop driving this new neutrino-hydrodynamical instability. Nevertheless, we cannot exclude that LESA is a numerical artifact and the final verdict depends on LESA being reproduced by 3D models with true multi-D transport (for discussions of multi-D transport effects in 3D, see Ref. [60], and in 2D, see Ref. [61]).

A directional dependence of this sort is not immediately obvious in the usual visualization of multi-D hydrodynamical simulations. Extracting the neutrino signal characteristics as a function of observer direction requires a significant amount of dedicated post-processing. In this sense, our study is also meant to encourage other SN modelers to show this sort of information which is important for neutrino signal detection and studies of flavor conversion. Our procedure for an efficient extraction of this information may be useful for other authors as well.

Of course, our discussion pertains exclusively to the SN accretion phase where hydrodynamical instabilities are a key element and which must ultimately lead to the explosion. For the initial collapse and bounce phase, perhaps up to about 100 ms after bounce, spherical symmetry remains a good approximation in discussing the neutrino emission. The neutrino signal during this early phase is surprisingly independent of model details [62, 63]. Likewise, after the explosion has taken off, the subsequent phase of proto-neutron star cooling is again governed by spherically symmetric emission. These three phases should be seen as distinct episodes, testing very different aspects of hydrodynamics as well as nuclear and particle physics.

Our paper begins in Sec. II with a summary of the main features of our SN models. In Sec. III we discuss the features of the neutrino signal from our three SN progenitors and the features of the LESA phenomenon in the presence of SASI. In Sec. IV we review the role of neutrino oscillations, while in Sec. V we focus on the detection perspectives of the signal modulation in IceCube and Hyper-Kamiokande. Discussion and conclusions will be presented in Sec. VI.

II. NUMERICAL SUPERNOVA MODELS

Our SN simulations were performed with the neutrino-hydrodynamics code PROMETHEUS-VERTEX. This SN simulation tool combines the hydrodynamics solver PROMETHEUS with the neutrino transport module VERTEX (see Refs. [55, 58] for more details and additional references). It includes a "ray-by-ray-plus" (RbR+), fully velocity and energy-dependent neutrino transport module based on a variable Eddington-factor technique that solves iteratively the neutrino energy, momentum, and Boltzmann equations [64, 65]. We employ state-of-the-art neutrino interaction rates [39, 65] and relativistic gravity and redshift corrections [64, 66]. The RbR+ description assumes the neutrino momentum distribution to be axisymmetric around the radial direction everywhere, implying that the neutrino fluxes are radial.

We have performed 3D simulations for the evolution of the 11.2 and 27 $M_\odot$ progenitors of Woosley, Heger and Weaver [67] and the 20 $M_\odot$ model of Woosley and Heger [68], using the high-density equation of state (EoS) of Lattimer and Swesty [69] with a nuclear incompressibility of $K = 220$ MeV. They were previously employed for 2D simulations [38–40, 70]. Seed perturbations for aspherical instabilities were imposed by hand 10 ms after core bounce by introducing random perturbations of 0.1% in density on the entire computational grid to seed the growth of hydrodynamic instabilities. None of these models led to successful explosions during the simulation period of about 350 ms for the 11.2 and 20 $M_\odot$ models and 550 ms for the 27 $M_\odot$ case, although explosions were obtained in the corresponding 2D simulations with the same microphysics. The postbounce hydrodynamics of the 27 $M_\odot$ model, in particular the prominent presence of SASI sloshing and spiral modes, was described in a previous paper [58], while more details on the hydrody-

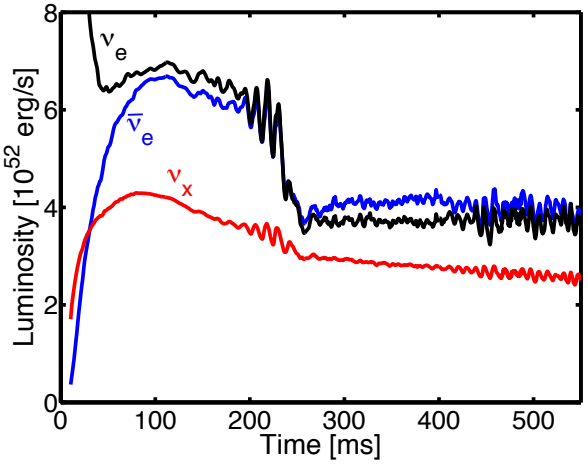

FIG. 1: Luminosity of the ν_e, $\bar{\nu}_e$ and ν_x species for our 27 $M_\odot$ simulation as measured by a distant observer with angular coordinates close to the plane of the spiral mode in the first SASI period.

namics of the 11.2 and 20 $M_\odot$ SN progenitors have been provided in our LESA paper [55].

The 20 and 27 $M_\odot$ models both show periods of strong SASI activity. In the former case, which was simulated until 550 ms post bounce (p.b.), a second SASI episode occurs after a period clearly dominated by convective overturn. On the other hand, the 11.2 $M_\odot$ model does not exhibit any clear evidence of SASI motions but develops the typical signatures of postshock convective overturn in the neutrino-heating layer.

We will usually show neutrino flux characteristics as they would be seen by a distant observer located at chosen angular coordinates in the coordinate system of the SN simulation. For any angular position, the neutrino luminosity reaching the observer is given by the superposition of the projected fluxes emitted under different angles, as described in Appendix A. Therefore, the observable neutrino fluxes are weighted hemispheric averages performed such as to include flux projection effects in the observer direction. The hemispheric averages, as expected, show smaller time variations than specific angular rays.

As a benchmark example, we show in Fig. 1 the luminosity for ν_e, $\bar{\nu}_e$ and $\nu_x = \nu_\mu$, ν_τ, $\bar{\nu}_\mu$ or $\bar{\nu}_\tau$ as a function of time, as seen by a distant observer with angular coordinates close to the plane of the SASI spiral mode. Large-amplitude, near-sinusoidal modulations of the neutrino signal occur in the interval 120–260 ms as imprinted by SASI. For 260–410 ms a convective phase occurs, followed by another SASI episode on a different plane with respect to the previous one. SASI modulations have a similar amplitude for ν_e and $\bar{\nu}_e$, while they are somewhat smaller for ν_x.

Figure 2 shows the properties of our 27 $M_\odot$ simulation, averaged over all directions, to mimic an equivalent spherically symmetric case. Of course, this average does not depend on observer-related projection effects. For the species ν_e, $\bar{\nu}_e$ and ν_x, we show the luminosity, average energy, and shape parameter α of the assumed spectral Gamma distribution (Appendix B). The fast time varia-

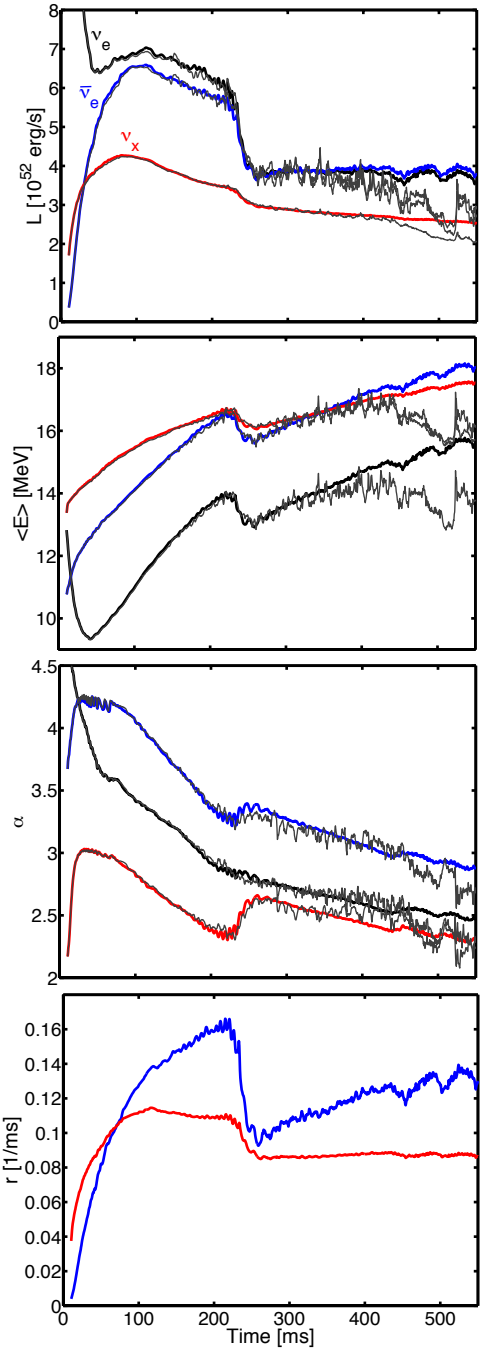

FIG. 2: Neutrino flux properties of our 27 $M_\odot$ case after integrating over all directions. For ν_e, $\bar{\nu}_e$ and $\bar{\nu}_x$ we show the luminosity, average energy and shape parameter α from 3D (in black, blue and red respectively) and 2D (in grey) simulations for comparison. The single-OM IceCube rate r in the bottom panel is without dead time for a SN distance of 10 kpc. Blue line: based on $\bar{\nu}_e$ flux without flavor oscillations. Red line: based on $\bar{\nu}_x$, i.e., assuming full flavor swap $\bar{\nu}_e \leftrightarrow \bar{\nu}_e$.

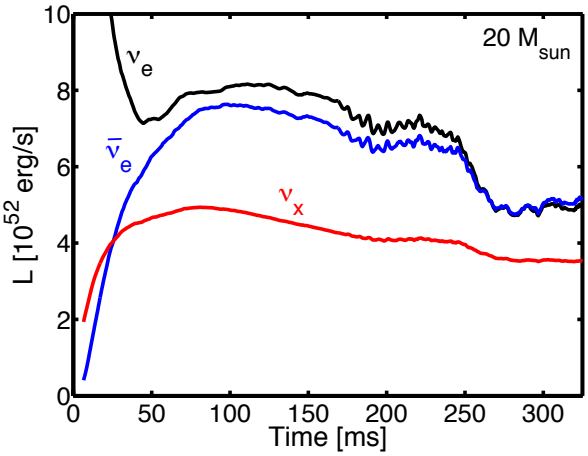

FIG. 3: Luminosity of the ν_e, $\bar{\nu}_e$ and ν_x species for our 20 $M_\odot$ simulation after integrating over all directions.

tions here have very small amplitude, i.e., convection and SASI activity do not strongly modulate the overall neutrino emission parameters—the modulations in various directions essentially cancel out.

The hierarchy of fluxes and average energies as well as the shape parameter correspond to what is expected. It is noteworthy, however, that the average $\bar{\nu}_e$ and $\bar{\nu}_x$ energies become very similar after around 220 ms, at the end of the first SASI episode, when the shock wave has considerably expanded. This feature has been seen in previous simulations [30, 37] too, and reflects the temperature increase in the settling, growing accretion layer on the proto-neutron star core. This accretion layer radiates mainly ν_e and $\bar{\nu}_e$ and downgrades the ν_x escaping from deeper layers in energy space [71]. The pronounced luminosity drop at ∼250 ms occurs because of the infall of the Si/SiO shell interface leading to strong shock expansion and therefore to a dramatic decrease of the mass accretion rate [58].

Although the difference between 2D and 3D models is not subject of our work, in Fig. 2 we show the corresponding 2D spectral parameters averaged over all directions. The 3D and 2D integrated quantities are very similar up to 300 ms when the 2D model explodes.

Figure 3 shows the luminosity of the ν_e, $\bar{\nu}_e$ and ν_x species for our 20 $M_\odot$ simulation, averaged over all directions to mimic an equivalent spherically symmetric case, for comparison with the top panel of Fig. 2. The hierarchy among the luminosities of different flavors as well as their behavior as a function of time is similar for both the 20 and 27 $M_\odot$ progenitors. However, the luminosities of ν_e and $\bar{\nu}_e$ are slightly higher for the 20 $M_\odot$ simulation. Despite the average over all directions, the integrated luminosities present residual sinusoidal modulations for $t \geq 160$ ms (i.e., during the SASI episode) with amplitude larger than for the 27 $M_\odot$ simulation (see Fig. 2, top panel) because the SASI activity is stronger for this SN model.

III. NEUTRINO SIGNAL FROM 3D MODELS

A. 11 $M_\odot$ progenitor

We now turn to a detailed discussion of the direction and time dependent features of the observable neutrino signal emitted by our 3D models. Beginning with the 11 $M_\odot$ progenitor, Fig. 4 shows the luminosity evolution, L, relative to the time-dependent average $\langle L \rangle$ over all directions, separately for ν_e, $\bar{\nu}_e$ and ν_x. This model does not show any SASI activity, but only small-amplitude, fast time variation caused by large-scale convective overturn. However after some 150 ms, the ν_e and $\bar{\nu}_e$ luminosities develop a quasi-stationary dipole pattern, representing the LESA effect discussed in our earlier paper [55].

The two observer directions shown in Fig. 4 (blue and magenta lines) are chosen on opposite sides of the SN along the LESA axis. The black curve represents a typical orthogonal direction, i.e., it is on the "LESA equator." The observer directions remain fixed in time whereas the LESA dipole direction slowly drifts, so in this sense these directions are not always exactly along the LESA axis or equator, respectively.

As discussed in our LESA paper [55], the sum of all flavor luminosities is almost independent of direction and the $\bar{\nu}_e$ and ν_e dipoles point in opposite directions. However, in a realistic detector, we measure only the $\bar{\nu}_e$ signal by inverse beta decay. Ignoring flavor oscillations, the measurable $L_{\bar{\nu}_e}$ could therefore differ by as much as 30% during the accretion phase, depending on the observer location, affecting the implied overall neutrino luminosity. Of course, what is really measured in a detector depends on flavor conversion which likely is a large effect. Since the $\bar{\nu}_x$ fluxes show a much weaker directional modulation, the real uncertainty between the measurement and the true 4π equivalent flux will be less dramatic.

In order to quantify the directional dependence of the neutrino signal, Fig. 5 shows the neutrino flux properties (luminosity, mean energy and the shape parameter α) for the three species along the same three directions chosen in Fig. 4, i.e., "Magenta," "Black" and "Blue" directions respectively named by the curves of the same colors shown in Fig. 4. We recall that the flux characteristics pertain to observers in those directions, i.e., they involve hemispheric averaging with appropriate flux projections. The small-amplitude "vibrations" of these parameters are caused by accretion variations associated with convective overturn.

The hierarchy among flavor-dependent luminosities along the three directions is slightly different. In particular, $L_{\nu_e} > L_{\bar{\nu}_e}$ along the "Magenta" direction, they are almost comparable along the "Black" direction, and $L_{\nu_e} < L_{\bar{\nu}_e}$ along the "Blue" direction, while the remaining neutrino flux properties exhibit the same hierarchy independently of the observer direction.

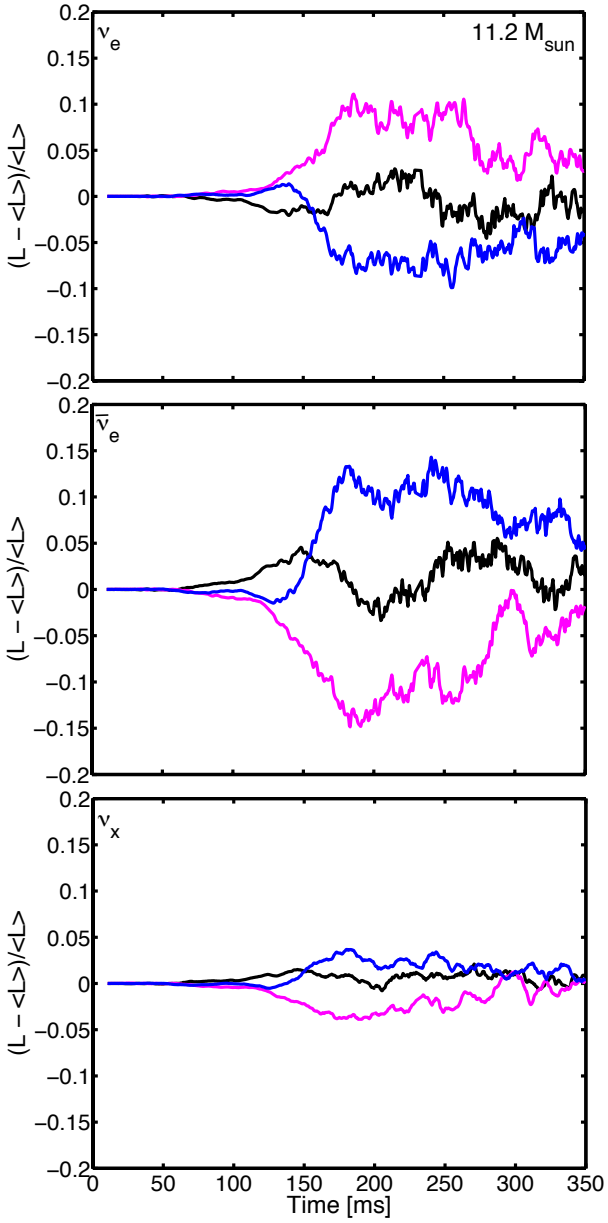

FIG. 4: Luminosity evolution for the 11.2 $M_\odot$ progenitor, separately for ν_e, $\bar{\nu}_e$ and ν_x, as seen by a distant observer, relative to $\langle L \rangle$, the time-dependent average over all directions. Blue and magenta curves: Observer location on opposite sides along the axis where the flux variations are largest. Black curve: One typical orthogonal direction where the variation is small. The large excursion of the blue and magenta lines represent the LESA phenomenon: The ν_e and $\bar{\nu}_e$ emission show a strong dipole pattern. The small-amplitude fast time variations are caused by large-scale convective overturn. There is no SASI activity in this model.

B. 20 and 27 $M_\odot$ progenitors

In contrast to the 11.2 $M_\odot$ case, the 20 and 27 $M_\odot$ progenitors show large-amplitude modulation of the neutrino signal due to SASI spiral modes, which cause accretion variations and corresponding fluctuations of the neutrino emission. The LESA phenomenon also occurs for these progenitors. Even though LESA persists during the phases of violent sloshing of the shock-wave radius, it is somewhat masked during the SASI episodes, as explained in our LESA paper [55]. We focus first on the 27 $M_\odot$ progenitor to facilitate comparison with the previous discussions of this model [28, 58].

Figure 7 shows the luminosity evolution, relative to the directional average, for the three flavors in analogy to Fig. 4. However, here we do not use the LESA axis and locate the observers in directions where the SASI amplitude is particularly large during the first SASI episode (light blue and violet lines) and a third direction where it is small (black). The SASI-implied modulations, on the other hand, are such that L_{ν_e} and $L_{\bar{\nu}_e}$ vary in phase with each other (see Fig. 8). The SASI variation of the neutrino signal is up to 15% for ν_e, even larger for $\bar{\nu}_e$, and still around 5% for ν_x.

While both SASI and convection can lead to large-scale shock deformations, SASI is distinguished by a characteristic quasi-periodic oscillatory nature. As discussed in Ref. [58], the SASI sloshing axis initially wanders and then stabilizes as the sloshing of the shock further grows in amplitude and violence. When SASI starts to grow vigorously, predominantly sloshing occurs, whereas later a transition to a spiral mode takes place, associated with a circular motion of the maximum shock radius. Both SASI and convective regimes are easily recognized in Fig. 7. For 120–260 ms, SASI sloshing and spiral modes occur, for 260–410 ms convection dominates, and then a second SASI episode takes place up to the end of our simulation (cf. Figs. 1, 2 and 6 of Ref. [58]).

The plane where spiral motions develop remains relatively stable until the maximum amplitude is reached and SASI dies down. During the first SASI spiral phase, the plane where it develops is roughly perpendicular to the vector $\mathbf{n} = (-0.35, 0.93, 0.11)$ in the SN simulation grid, i.e., there is no alignment with the axis of the spherical polar grid [58]. The second SASI phase develops in a plane different from the first one. Therefore, the three fixed directions shown in Fig. 7 are no longer optimal relative to a maximum SASI effect.

In Fig. 8 the luminosity evolution, relative to the directional average, is shown as a function of time for the three flavors, along the direction plotted in violet in Fig. 7. The LESA phenomenon, while somewhat masked during the SASI episodes, clearly appears during the convective phase between the SASI episodes, in the form of a hemispheric asymmetry between ν_e and $\bar{\nu}_e$ luminosity. The relative LESA amplitude of $\bar{\nu}_e$ is opposite in sign to the one of ν_e and the amplitude for ν_x is smaller, with its sign correlated with the one of $\bar{\nu}_e$. The SASI modulations, on the other hand, have the same sign for all flavors, but a smaller amplitude for ν_x.

In order to discuss the directional dependence of the SASI modulation of the neutrino signal, Fig. 6 shows the neutrino flux properties (luminosity, mean energy and

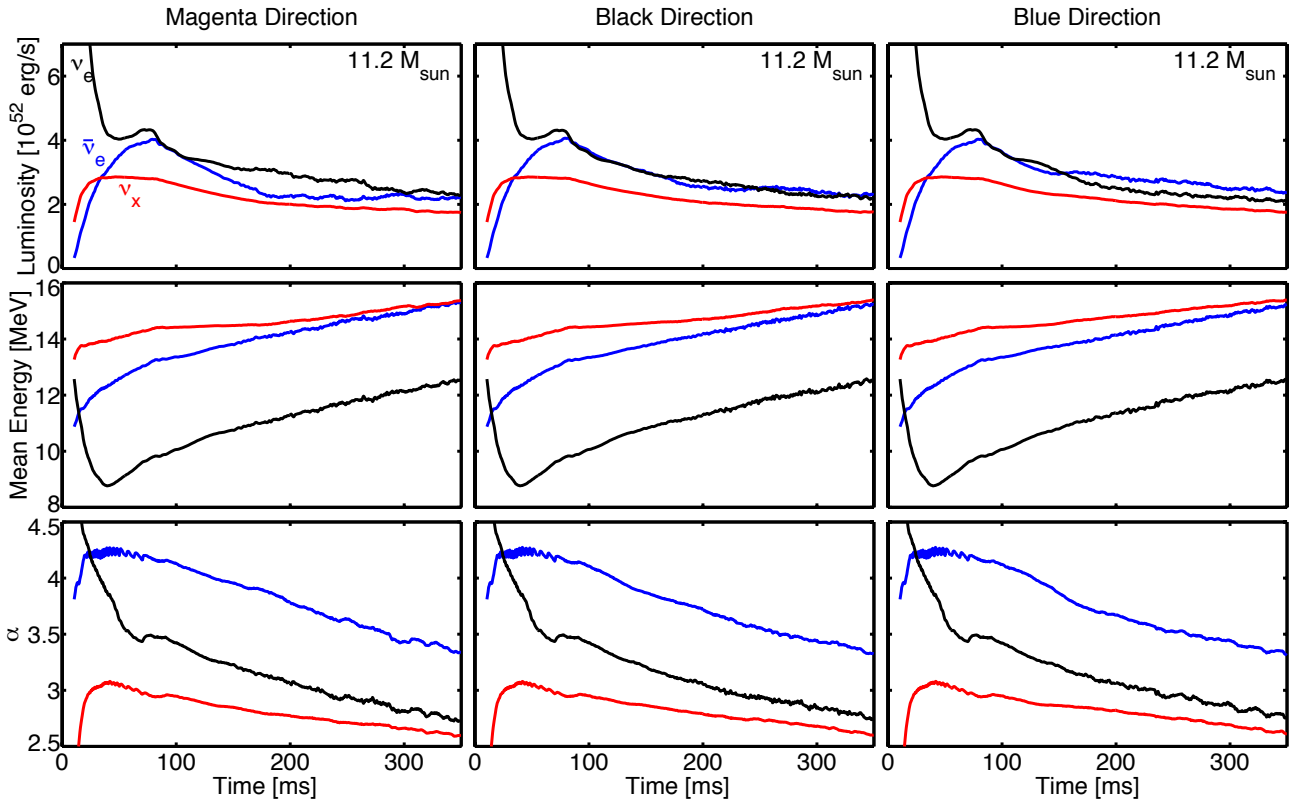

FIG. 5: Evolution of neutrino flux properties for the 11.2 $M_\odot$ progenitor as seen from a distant observer. For ν_e, $\bar{\nu}_e$ and ν_x we show the luminosity, average energy and shape parameter α. The "Magenta" and "Blue" directions are opposite along the LESA axis, corresponding to the magenta and blue curves in Fig. 4, whereas the "Black" direction is on the LESA equator (black in Fig. 4).

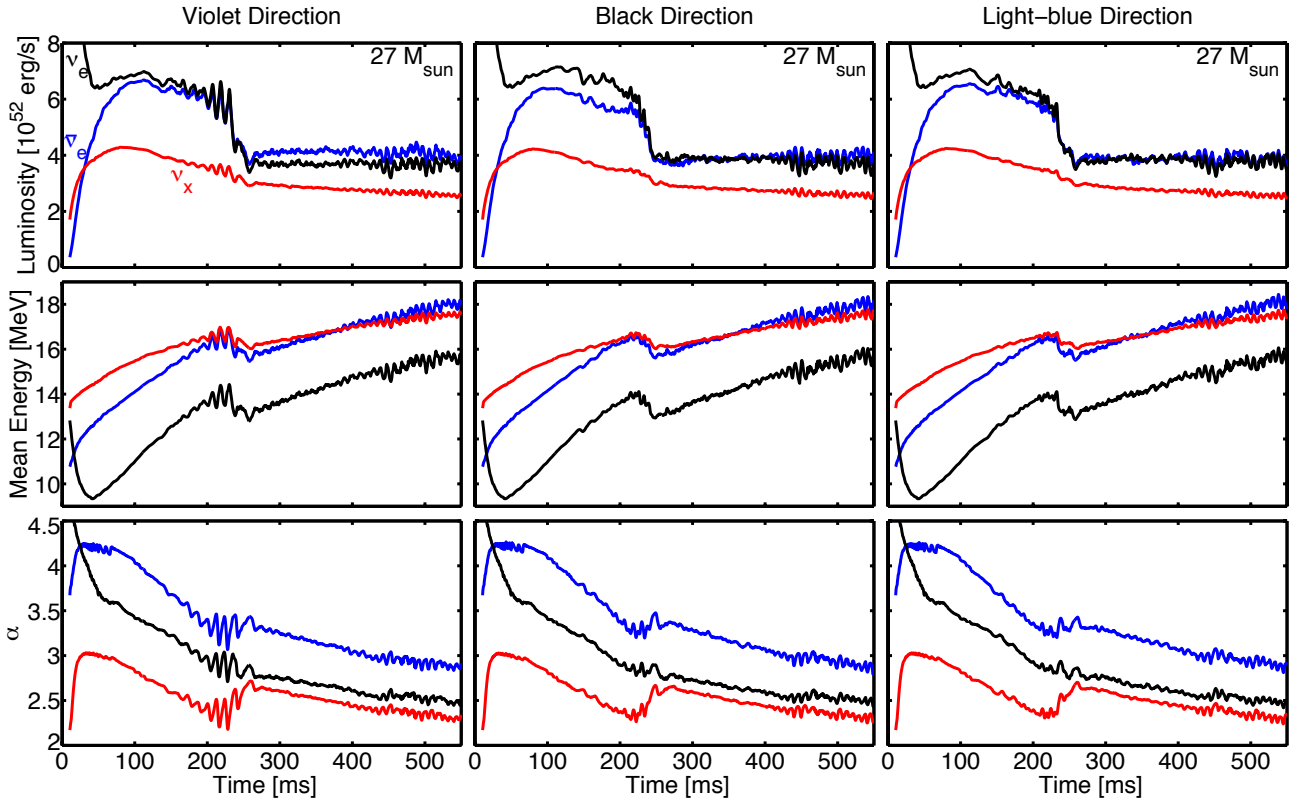

FIG. 6: Same as Fig. 5, but for the 27 $M_\odot$ progenitor. The "Violet," "Black" and "Light Blue" directions here correspond to the curves of the same color in Fig. 7 that were chosen to show large and small SASI amplitudes, respectively.

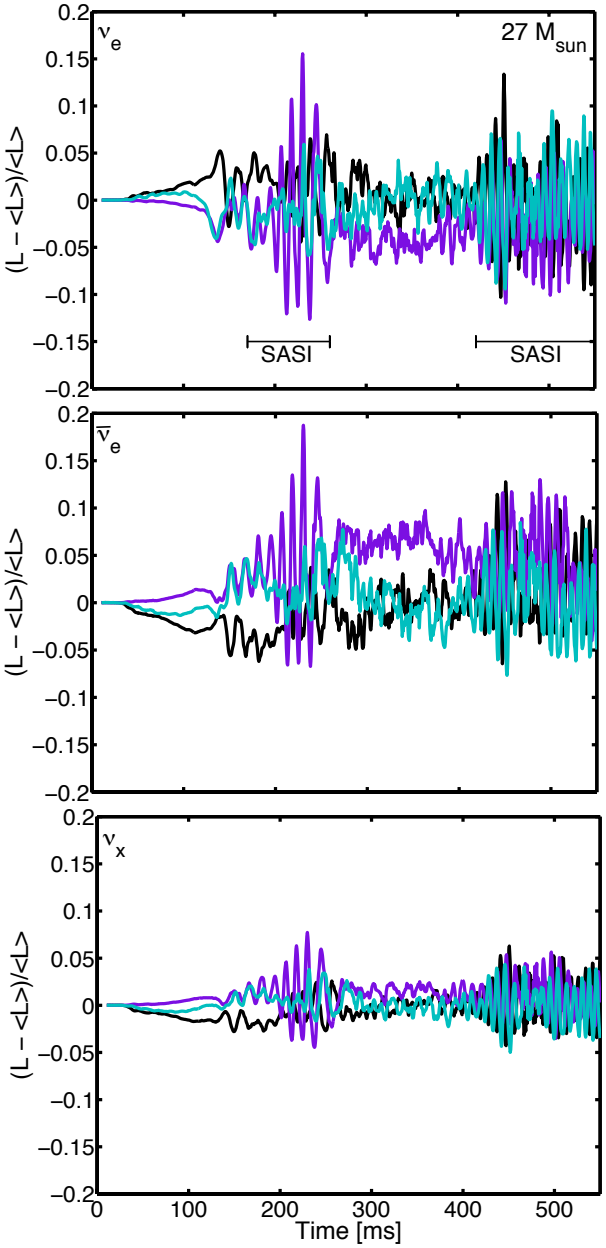

FIG. 7: Luminosity evolution for the 27 $M_\odot$ progenitor, separately for ν_e, $\bar{\nu}_e$ and ν_x, as seen by a distant observer, relative to $\langle L \rangle$, in analogy to Fig. 4. The light blue and violet curves refer to observer locations in opposite directions approximately within the plane where SASI develops. The black line refers to a location of the observer far from the SASI plane where the modulation of the neutrino signal due to SASI is smaller during the first SASI episode.

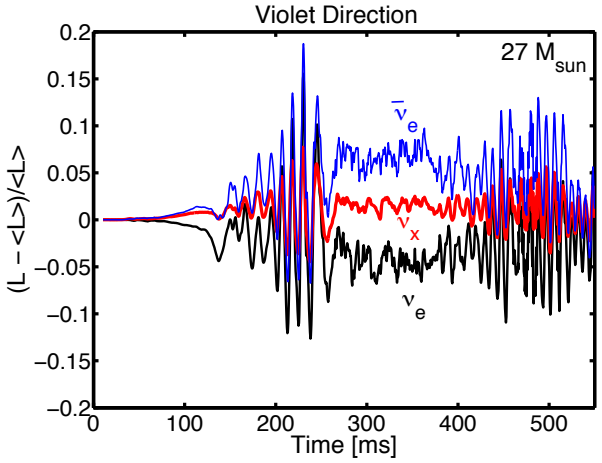

FIG. 8: Luminosity evolution relative to $\langle L \rangle$ for the 27 $M_\odot$ progenitor for the three species, as seen by a distant observer, along the "Violet" direction, corresponding to the curve of this color in Fig. 7. Between SASI episodes, we see clear evidence for the LESA asymmetry, although the chosen direction does not coincide with the LESA axis.

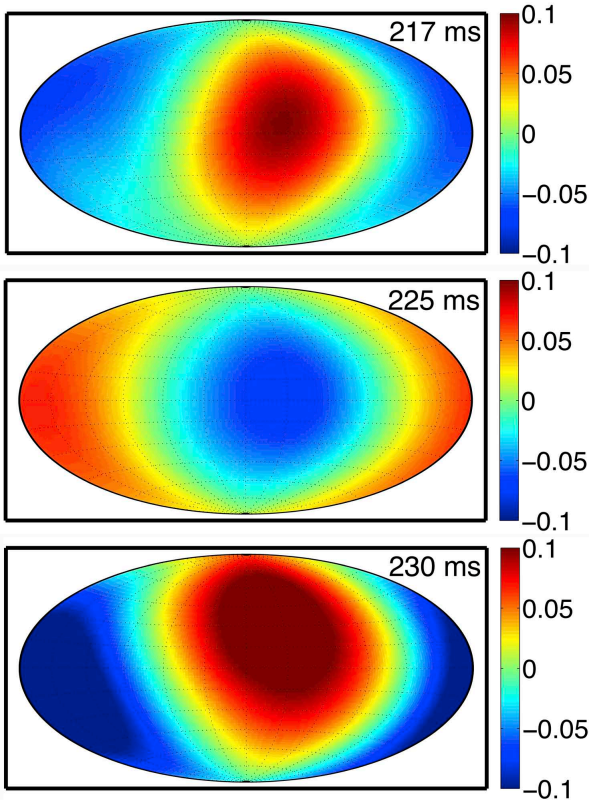

FIG. 9: Sky maps of $L_{\bar{\nu}_e}$ relative to the 4π average for the 27 $M_\odot$ SN progenitor at $t = 217$, 225 and 230 ms, corresponding to subsequent SASI maxima and minima.

shape parameter α) for the three flavors along the same three directions, respectively corresponding to the violet, black, and light blue curves in Fig. 7 and named by color. Although the neutrino flux properties are similar for all directions, the modulation of the signal along "Black" and "Light Blue" directions is much less pronounced during the first SASI episode than the modulation along the "Violet" direction.

Figure 9 shows sky maps of the relative luminosity of $\bar{\nu}_e$ for $t = 217$, 225 and 230 ms, i.e., corresponding to subsequent SASI maximum and minimum signal ampli-

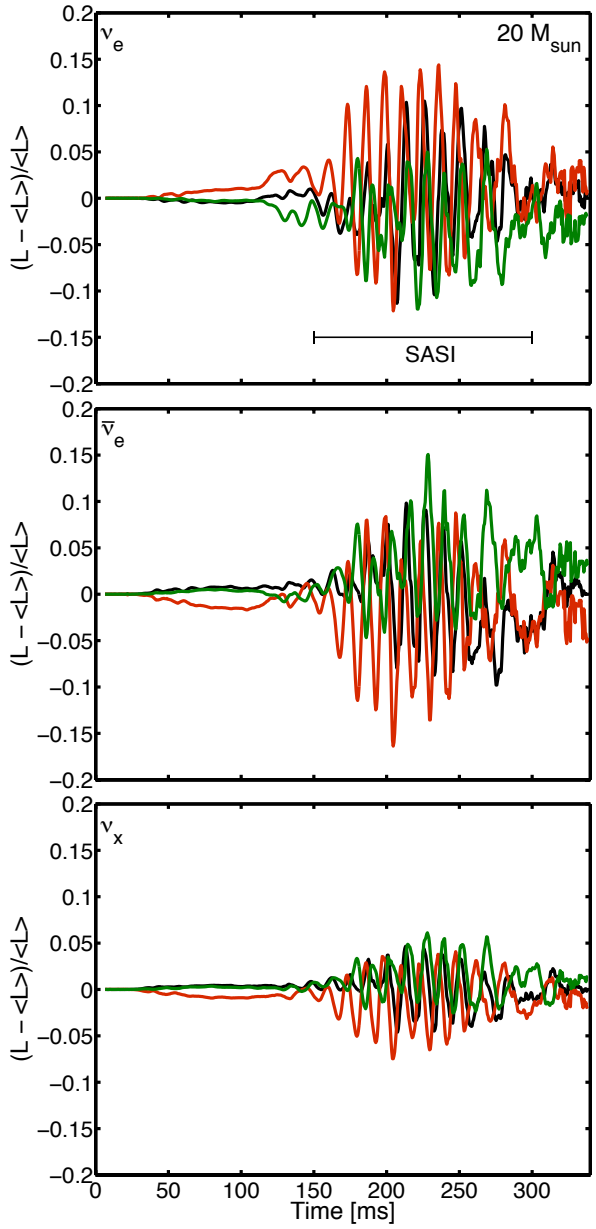

FIG. 10: Variation of the luminosity for $\nu_e, \bar{\nu}_e$ and ν_x relative to the one computed as average over all directions for the 20 $M_\odot$ SN progenitor at 10 kpc in analogy to Fig. 4. The green and orange curves refer to locations of the observer close to the plane where SASI develops and on opposite sides of the emitting sphere. The black line refers to a location of the observer far from the SASI plane where the modulation of the neutrino signal due to SASI is smaller.

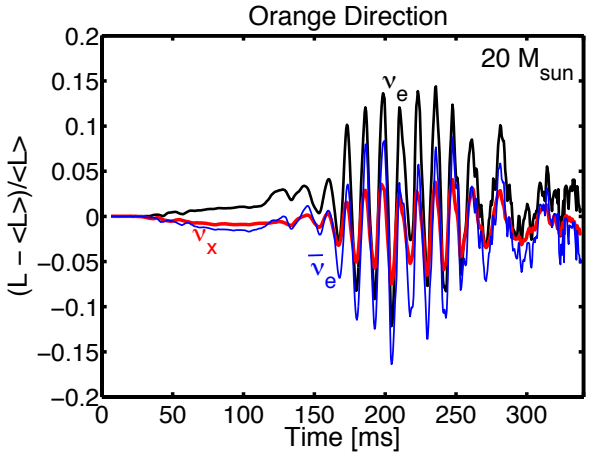

FIG. 11: Luminosity evolution relative to $\langle L \rangle$ for the 20 $M_\odot$ progenitor for the three species, as seen by a distant observer along the "Orange" direction, corresponding to the curve of this color in Fig. 10. See Fig. 8 for comparison.

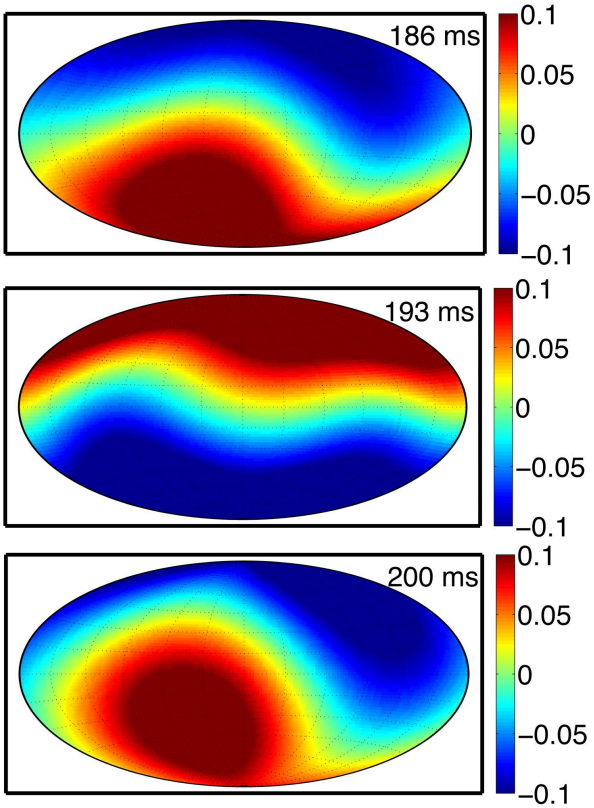

FIG. 12: Sky maps of $L_{\bar{\nu}_e}$ relative to the 4π average for the 20 $M_\odot$ SN progenitor at $t = 186$, 193 and 200 ms, corresponding to subsequent SASI maxima and minima in analogy to Fig. 9.

tudes. Comparing the three snapshots there is again a total variation of $\sim 20\%$ for the different angular positions. Looking at the hottest and coldest spot in the three time slices, it is clear how the SASI sloshing motions proceed.

We repeat the same analysis as before for the 20 $M_\odot$ progenitor. Figure 10, in analogy to Fig. 7, shows the relative luminosity. This progenitor exhibits only one SASI episode for $t \geq 160$ ms, lasting for a longer time than for the 27 $M_\odot$ progenitor. The SASI-implied modulations are again such that L_{ν_e} and $L_{\bar{\nu}_e}$ vary in phase with each other, as clearly visible in Fig. 11. Traces of LESA ap-

pear in the hemispheric asymmetry between the ν_e and $\bar{\nu}_e$ luminosity, especially before SASI sets in ($t < 160$ ms) when the relative variation of $\bar{\nu}_e$ is opposite in sign to the one of ν_e. We find maximum fluctuations of the signal of 17% and minimum of 7%. Figure 12, similar to Fig. 9, shows sky maps of the relative $\bar{\nu}_e$ luminosity for three snapshots ($t = 186$, 193 and 200 ms) corresponding to the SASI maximum and minimum signal amplitudes. As for the 27 $M_\odot$ SN progenitor, a total variation of $\sim 20\%$ for the different angular positions occurs. The SASI spiral mode develops in a plane perpendicular to $\mathbf{n} = (-0.56, -0.81, -0.20)$ in the SN simulation grid, i.e., in a different plane than in the 27 $M_\odot$ case, as evident from a comparison of Figs. 9 and 12. In fact the SASI plane is randomly selected and bears no relation to the numerical grid in the case of a non-rotating model.

C. The LESA phenomenon in presence of SASI

The LESA phenomenon is characterized by a maximum of the ν_e emission coincident with a minimum of the $\bar{\nu}_e$ emission (i.e., the amplitude of the ν_e emission is anti-correlated with the amplitude of the $\bar{\nu}_e$ emission), whereas SASI is responsible for correlating the amplitude variations of the ν_e and $\bar{\nu}_e$ signals (see Figs. 7, 8, 10, and 11). In order to investigate in greater detail the LESA phenomenon in the presence of SASI for our two heavier progenitors, we consider the LESA dipole, i.e., the dipole component of the lepton number flux (ν_e minus $\bar{\nu}_e$), following the definition adopted in Sec. 3.1 of Ref. [55] (see also their Fig. 3), and the SASI dipole, i.e., the dipole component of the neutrino energy flux of all flavors ($\nu_e + \bar{\nu}_e + 4\ \nu_x$). Note that we choose the total neutrino energy flux to define the SASI dipole instead of the total number flux because SASI modulates the total energy flow, including the mean neutrino energies [28]. The monopole component of the total neutrino energy flux of all flavors corresponds to the sum of luminosities for all flavors, as shown in Figs. 2 (top panel) and 3 for the 27 $M_\odot$ and 20 $M_\odot$ SN progenitors, respectively.

Figure 13 shows the length of the dipole vector of the neutrino energy flux of all six neutrino species (top panels) and of the dipole component of the lepton number flux (bottom panels) for the 27 $M_\odot$ (left) and for the 20 $M_\odot$ (right) progenitors as a function of time. Note that the LESA dipole is different from zero, even during the SASI episodes [55]. This means that the LESA mechanism is active during SASI episodes, even if the LESA dipolar behavior is not clearly visible in the neutrino signal in Figs. 7, 8, 10, and 11 because it is masked by strong SASI modulations.

The "SASI dipole" of the 27 $M_\odot$ progenitor does not completely vanish between SASI episodes because large-scale convection also causes an overall emission dipole. During the first SASI episode it increases strongly, reaching its maximum around 200 ms where it is about 16% of its monopole (total energy flux, i.e., the sum of the luminosities as plotted on the top panel of Fig. 2). During the second SASI phase it is at most 10% of its monopole. On the other hand, the LESA dipole quickly grows up to 150 ms. The LESA dipole is almost two times the monopole at about 500 ms. The SASI activity of the 20 $M_\odot$ model is more pronounced compared to the the 27 $M_\odot$ simulation and the SASI dipole is correspondingly larger. However, in relative terms it also reaches a maximum of 16% of the monopole strength at 180 ms and then decreases. On the other hand, the ratio between the LESA dipole and monopole is maximum at 280 ms and is about 1.4. It is interesting to notice that the general trend as a function of time is the same between LESA and SASI dipoles, but it is strongly progenitor dependent. In particular the dipole grows during the SASI activity for the 20 $M_\odot$ SN progenitor, while it is on average stationary during SASI for the 27 $M_\odot$ SN progenitor.

Figure 14 shows the track of the LESA dipole in gray and the SASI dipole in blue hues during the SASI episodes for the 27 $M_\odot$ (left) and for the 20 $M_\odot$ (right) SN progenitors, in order to investigate a possible correlation between the LESA dipole and the plane of the SASI sloshing and spiral modes. While for the 27 $M_\odot$ case, the SASI spiraling drives the LESA dipole to wander in the SASI plane, this does not happen for the 20 $M_\odot$ SN progenitor. The neutrino SASI dipole trajectory closely reproduces the shock-deformation trajectory shown in Fig. 8 of Ref. [55].

The LESA dipole direction as well as the SASI dipoles are progenitor dependent (see also Fig. 3 of Ref. [55]), and none of them are correlated with the numerical grid of the simulation. The mutual interaction between SASI and LESA seems to be strongly progenitor dependent, although from this preliminary analysis it is clear that these are two separate phenomena. We here refrain from drawing any firm conclusion on the interaction between LESA and SASI since a much deeper understanding of the LESA phenomenon and its origin is required and hydrodynamical simulations of more SN progenitors are needed to favor a better understanding of the coexistence between the two phenomena.

IV. FLAVOR OSCILLATIONS

Neutrino transport in SN models is treated in the weak-interaction basis of flavors. In our three-species treatment, we use ν_e, $\bar{\nu}_e$ and ν_x, neglecting weak-magnetism effects that distinguish between neutral-current scattering of ν_μ (ν_τ) and $\bar{\nu}_\mu$ ($\bar{\nu}_\tau$). We also ignore the possible presence of muons that would allow charged-current processes for ν_μ and $\bar{\nu}_\mu$ in the deep interior of the proto-neutron star. Most importantly, we ignore flavor conversion caused by flavor mixing. The justification for this simplification is the strong matter effect that effectively "de-mixes" neutrinos, i.e., the propagation eigenstates essentially coincide with the weak-interaction eigenstates [72].

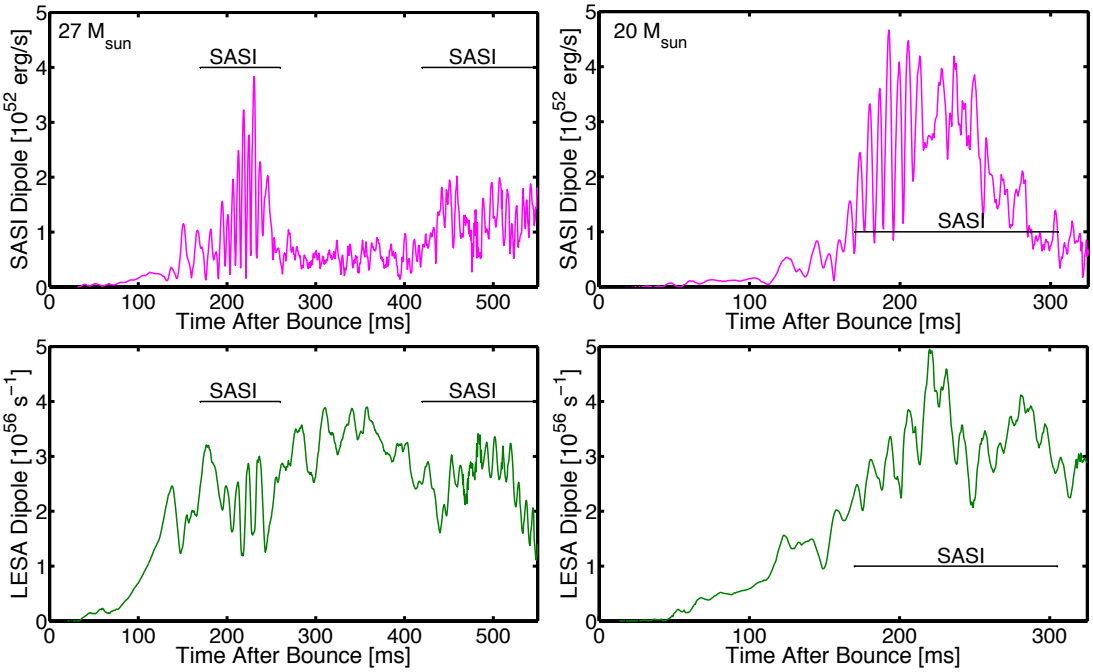

FIG. 13: SASI vs. LESA dipole as a function of time for the 27 $M_\odot$ (left) and the 20 $M_\odot$ (right) simulations. We describe the SASI dipole (top panels) in terms of the neutrino energy flux of all six neutrino species. For the 27 $M_\odot$ model (left), it reaches a maximum of 0.16 relative to its monopole at 200 ms, while for the the 20 $M_\odot$ model (right) the maximum is reached at 180 ms with the same relative strength. The LESA dipole (bottom panels) is described in terms of the lepton-number flux (ν_e minus $\bar{\nu}_e$) and reaches a relavive maximum of 2 times the monopole at 500 ms for the 27 $M_\odot$ case (left) and of 1.4 times the monopole at 280 ms for 20 $M_\odot$.

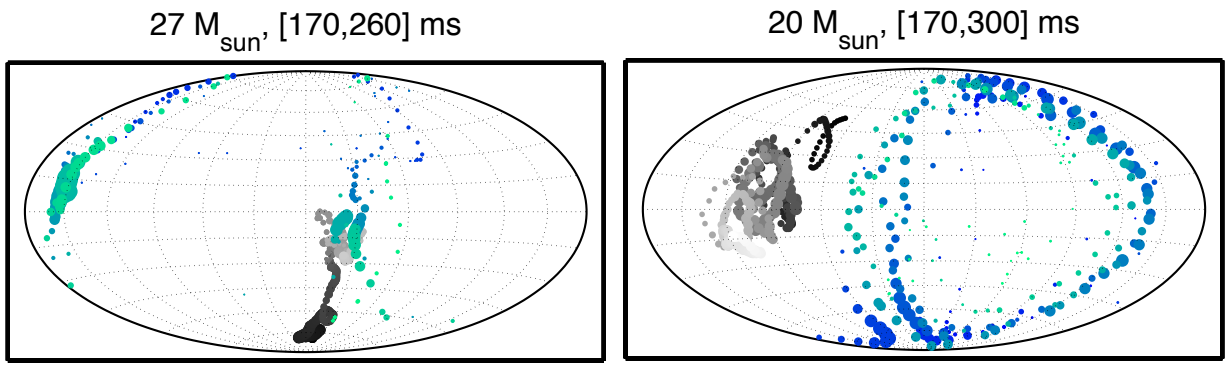

FIG. 14: Sky maps showing the evolution of the LESA direction (i.e., direction of the dipole of the lepton number flux) in gray color scale and of the SASI direction (i.e., direction of the dipole of the neutrino energy flux of all six neutrino species) in blue color scale for the 27 $M_\odot$ SN progenitor (left) and the 20 $M_\odot$ SN progenitor (right) during the periods of strongest SASI activity. The color hues become lighter as time progresses. The size of the dots scales with the length of the plotted dipole vector. While for the 27 $M_\odot$ SN progenitor the LESA dipole is close to the SASI plane, for the 20 $M_\odot$ case they are nearly perpendicular to each other and no clear correlation exists between the LESA dipole direction and the SASI one.

However, as neutrinos stream away from the SN core, the matter effect decreases and eventually flavor conversion becomes important. What is measured in a detector crucially depends on neutrino flavor oscillations along the way.

In the simplest traditional picture, the slowly-varying matter profile provides for adiabatic flavor conversion, the so-called Mikheev-Smirnov-Wolfenstein (MSW) effect [72, 73]. In particular, the recent measurement of the third mixing angle $\sin^2(2\Theta_{13}) = 0.095 \pm 0.010$ [74], being fairly large, implies that the entire three-flavor conversion process would indeed be adiabatic [75]. For the normal neutrino mass hierarchy (NH), the $\bar{\nu}_e$ survival probability is $\bar{p}_{\rm NH} = \cos^2\Theta_{12} \sim 0.70$, whereas for the inverted ordering (IH) it is $\bar{p}_{\rm IH} = 0$ [75]. Therefore, a detector measuring $\bar{\nu}_e$ by inverse beta-decay (IBD) will see

in NH a superposition of roughly 70% of the original $\bar{\nu}_e$ flux spectrum with 30% of the $\bar{\nu}_x$ flux spectrum, whereas in IH it will detect the original $\bar{\nu}_x$ flux spectrum at the source.

This simple prediction can get strongly modified by two effects. The density profile can be noisy and show significant stochastic fluctuations [51, 76–79] that can modify the adiabatic conversion [80–85]. Such effects would be especially expected in the turbulent medium behind the shock wave, i.e., the relevance pertains in particular to neutrino propagation after the explosion has set in and the shock wave travels outward. However, we are here concerned with the standing-shock phase and flavor conversion outside of the shock-wave radius.

Of greater importance is then the impact of neutrino-neutrino refraction which can lead to self-induced flavor conversion, usually at a smaller radius than the MSW effect [86]. It can put the MSW result effectively upside down and can lead to novel spectral features (spectral splits) [87–93]. On the other hand, self-induced flavor conversion can be suppressed by the "multi-angle matter effect" [94] and this may be typical in many cases, re-instating the traditional scenario [95–97]. On the other hand, what exactly happens when self-induced conversion is not suppressed remains poorly understood because of a number of complications that have only recently been appreciated [98–106]. In addition, the direction-dependent neutrino flux properties and especially the LESA phenomenon throw in additional uncertainties that have not been studied yet.

In this situation we can but state that the $\bar{\nu}_e$ flux arriving at the detector will be some superposition, possibly depending on energy, of the original $\bar{\nu}_e$ and $\bar{\nu}_x$ flux spectra. We therefore consider two extreme cases. One is that the detector measures the original $\bar{\nu}_e$ flux, the other assumes a complete flavor swap and the detector measures what was the $\bar{\nu}_x$ flux at the source.

V. DETECTION OF SIGNAL MODULATIONS

A. Detector Models

Detecting the SASI-imprinted modulations in the high-statistics neutrino signal of the next galactic SN would go a long way in studying SN hydrodynamics. What are the opportunities for such a detection?

In the largest operating detector, IceCube, and the future Hyper-Kamiokande, neutrinos are primarily detected by IBD, $\bar{\nu}_e + p \to n + e^+$, through the Cherenkov radiation of the final-state positron. We will ignore the small additional contribution from elastic scattering on electrons. The signature for fast time variations is limited by random fluctuations (shot noise) of the detected neutrino time sequence.

In IceCube [4], usually at most one Cherenkov photon from a given positron is detected, i.e., every measured photon signals the arrival time of a neutrino and in this sense provides superior signal statistics. In rare cases, two or more photons from a single neutrino are detected, depending on neutrino energy, allowing one to extract interesting spectral information from time-correlated photons [5], but this intriguing effect is not of direct interest here. The instantaneous signal count rate caused by IBD in a single optical module (OM) is [4]

$$r_{\rm IBD} = n_p \int dE_e \int dE_\nu \, F_{\bar{\nu}_e}(E_\nu)\, \sigma'(E_e, E_\nu)\, N_\gamma(E_e)\, V_\gamma^{\rm eff}, \tag{1}$$

where $n_p = 6.18 \times 10^{22}$ cm^{-3} is the number density of protons in ice (density 0.924 g cm^{-3}), E_e is the final-state positron energy, $V_\gamma^{\rm eff} = 0.163 \times 10^6$ cm^3 the average effective volume for a single photon detection, $N_\gamma(E_e) = 178\, E_e/{\rm MeV}$ is the energy-dependent number of Cherenkov photons, and $\sigma'(E_e, E_\nu) = d\sigma(E_e, E_\nu)/dE_e$ is the IBD cross section, differential with respect to the positron energy.

We correct the positron energy, $E_e \to E_e + 1$ MeV, because gamma rays from positron annihilation and neutron capture produce additional recorded energy [4]. Moreover, the IceCube rate from IBD is about 94% of the total, so we apply a correction factor

$$r = r_{\rm IBD}/0.94 \tag{2}$$

to account approximately for all channels.

Every OM shows a background rate of around 540 Hz, including correlated events. Introducing an artificial dead time of $t_{\rm dead} = 250$ μs after every hit reduces the background to a single rate of about 286 Hz at the cost of about 13% dead time. More specifically, the signal reduction by this dead-time effect is $0.87/(1 + r\, t_{\rm dead})$. Therefore, the overall SN signal rate is

$$R_{\rm IC} = N_{\rm OM}\, \frac{0.87\, r}{1 + r\, t_{\rm dead}}\,, \tag{3}$$

where $N_{\rm OM} = 5160$ is the number of OMs in IceCube.

In previous studies of the IceCube potential for detecting fast signal variations [25, 26], these various corrections had not been included. Moreover, a simple approximate expression for the IBD cross section was used. As in our companion *Physical Review Letter* [28], we here use the IBD cross section provided in Ref. [107], which includes recoil, the neutron-proton mass difference, the positron mass, and nucleon form factors. If the $\bar{\nu}_e$ spectrum is described by a Gamma distribution (see Appendix B), the final-state positrons also follow such a distribution with good approximation. In Appendix B we give analytic approximation formulas for the spectral parameters of the detected positrons in terms of those of the primary $\bar{\nu}_e$.

For the example of our $27\,M_\odot$ model, Fig. 2 (bottom panel) shows the single-OM IceCube rate r as defined in Eq. (2) without dead-time effect. We show r for $\bar{\nu}_e$, ignoring flavor oscillations, and also for $\bar{\nu}_x$ under the assumption of a full flavor swap $\bar{\nu}_e \leftrightarrow \bar{\nu}_x$. The maximum rate is around 170 Hz, somewhat larger than half of the

background rate, so that $r\,t_{\rm dead} \sim 0.04$. In this case, dead-time effects reduce the overall signal to about 84% of the raw rate.

Incorporating dead time, the average single-OM background rate is 286 Hz. After multiplying with $N_{\rm OM} = 5160$ we find an overall background rate of

$$R_{\rm bkgd} = 1.48 \times 10^3 \ {\rm ms}^{-1} \,. \tag{4}$$

For a SN at 10 kpc, this is about twice a typical signal rate. The detectability of fast time variations is limited by random signal fluctuations (shot noise) which originates from both the signal itself and fluctuations of the background rate.

As for Hyper-Kamiokande [8], a next-generation megaton water Cherenkov detector, we focus on the number of IBD events, expecting a correction of a few percent due to the other neglected channels. The expected rate is

$$R_{\rm HK} = N_p \int dE_e \int dE_\nu \, F_{\bar\nu_e}(E_\nu)\, \sigma'(E_e, E_\nu), \tag{5}$$

where $N_p = 4.96 \times 10^{34}$ is the number of protons for a 0.74 Mton Cherenkov detector [8]. The advantage relative to IceCube is that such a detector is essentially background free and, as a plus, will provide event-by-event energy information. We found that although the expected rate as function of time is almost three times lower than the IceCube rate [28], the expected Hyper-Kamiokande rate has the same modulation of the signal with slightly lower amplitude. We also noticed (results not shown here) as convolving the expected signal rate with powers of the energy, that the amplitude of the sinusoidal modulations is enhanced.

B. Detection Perspectives

Figure 15 shows the expected IceCube and Hyper-Kamiokande rates for 27, 20 and 11.2 $M_\odot$ SN progenitors, respectively, from left to right, at a distance of 10 kpc and for $\bar\nu_e$ and ν_x (assuming full swap by flavor conversion) fluxes. For the progenitors where SASI develops (27 and 20 $M_\odot$ progenitors), we show the signal as seen by a distant observer close to the SASI spiral plane where the signal modulations are large. The IceCube rate was defined in Eq. (3) and the Hyper-Kamiokande one in Eq. (5).

The relative amplitude of the SASI modulations is similar in the $\bar\nu_e$ and $\bar\nu_x$ channels, although the $\bar\nu_x$ rate is always lower that the $\bar\nu_e$ one. The origin of this effect is that, although the luminosities show different amplitudes of SASI modulation (Fig. 1), the $\bar\nu_x$ spectrum is less pinched than the $\bar\nu_e$ one (see α's for $\bar\nu_e$ and ν_x in Fig. 2). As discussed in our earlier paper [28], in spite of shot noise, an observer located along an optimal direction will be able to detect SASI modulations out to a distance of 20 kpc (cf. Fig. 1 of Ref. [28]). Note that IceCube and Hyper-Kamiokande offer complementary information since IceCube will be more suitable for SN at small distances where the shot noise is smaller. Hyper-Kamiokande will be more useful at larger distances because it is background free and the shot noise is dominated by fluctuations of the signal itself [28].

As shown in Fig. 7 (black line), SASI has not the same intensity along all the directions and can be very weak. In order to characterize where, on average, the modulations of the neutrino signal due to SASI are stronger and therefore where an observer has more chances to detect it, we define the following standard deviation of the IceCube rate for each angular position of the observer [28]

$$\sigma^2 = \int_{t_1}^{t_2} dt \, \left(\frac{R - \langle R \rangle}{\langle R \rangle} \right)^2 \,, \tag{6}$$

where $\langle R \rangle$ is the time-dependent average over all directions.

Figure 16 (upper panel) shows a sky-map of $\sigma/\sigma_{\rm max}$ with $\sigma_{\rm max}$ the maximum of σ during the first SASI window of the 27 $M_\odot$ SN progenitor, i.e., integrating over the time interval 120–250 ms. It is clear that the SASI modulations are on average stronger, and will be experimentally observable, for an extended region close to the SASI spiral plane, roughly corresponding to 60% of possible observer locations. The regions of strong SASI modulations visible in Fig. 16 correspond to the hottest and coldest regions in Fig. 9. Of course, for several SASI episodes or a strong drift of the main plane, some part of the SASI activity may become visible in a larger fraction of all observer directions at different times.

Figure 15 (middle panel) shows the IceCube and Hyper-Kamiokande rates for the 20 $M_\odot$ SN progenitor along one of the directions where SASI modulation of the neutrino signal is strong. Only one SASI phase occurs for this progenitor and SASI is somewhat stronger than for the 27 $M_\odot$ SN progenitor. Indeed, the detection rate for this progenitor is slightly higher than for the 27 $M_\odot$ case.

Figure 16 (bottom panel) shows the sky-map of $\sigma/\sigma_{\rm max}$ for the SASI episode 150–330 ms of the 20 $M_\odot$ star. Comparing the two panels of Fig. 16, we see that, as already pointed out in Sec. III B, SASI develops for the 20 $M_\odot$ progenitor on a different plane than for the 27 $M_\odot$ case. Therefore, the optimal observer directions to detect SASI effects are almost perpendicular in the two models.

In our earlier paper [28], we have considered the power spectrum of the IceCube rate for all the three studied SN progenitors. One finds a strong peak at $f \simeq 80$ Hz for the 27 and 20 $M_\odot$ cases, corresponding to the typical SASI frequency. This frequency equals the one that describes large-amplitude fluctuations of the low spherical harmonics SASI amplitude vector in Fig. 2 (right panel on the top) of Ref. [58]. It is also basically understood from analytic and numerical studies of the linear growth regime of the SASI, and it is roughly the inverse of the advection timescale plus the sound travel timescale (see Eq. 2 of Ref. [28]). Both of these timescales only depend on shock radius and neutron-star radius [28, 53].

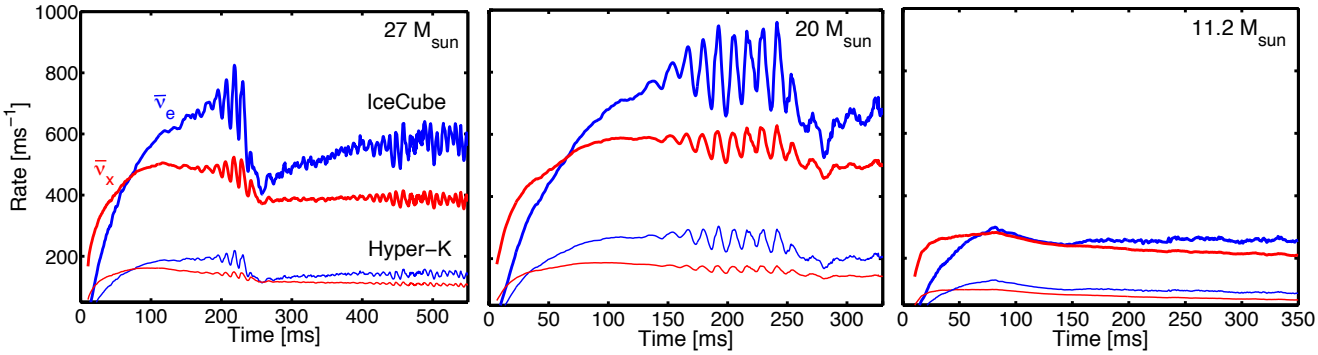

FIG. 15: IceCube and Hyper-Kamiokande detection rates R for our 27, 20 and 11.2 $M_\odot$ SN progenitors at a distance of 10 kpc. The rates are shown for $\bar{\nu}_e$ and for $\bar{\nu}_x$ (i.e., assuming full swap by flavor conversion). For the 27 and 20 $M_\odot$ progenitors, the observer direction is close to the SASI plane where the signal modulation is strong.

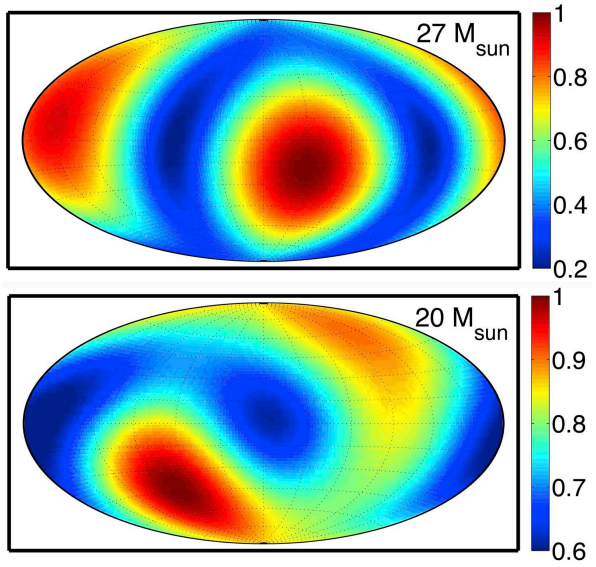

FIG. 16: Sky-map of $\sigma/\sigma_{\rm max}$ with σ^2 defined in Eq. (6). Top panel: 27 $M_\odot$ progenitor during the first SASI phase (120–250 ms). Bottom panel: 20 $M_\odot$ progenitor during 150–330 ms.

VI. DISCUSSION AND SUMMARY

The first 3D full-scale hydrodynamical SN simulations with sophisticated neutrino transport are now available for three SN progenitors with masses 11.2, 20 and 27 $M_\odot$, respectively. In a series of papers, we have explored the neutrino emission properties of these models and in particular the dependence on observer direction and the time variability of the signal and opportunities to measure them in large-scale detectors such as IceCube and the future Hyper-Kamiokande.

The first important point was made in our companion *Physical Review Letter* [28] where we emphasized the appearance of pronounced SASI activity in our two heavier progenitors. The question if SASI indeed appears in 3D models or if it would be suppressed by convective overturn had been debated among SN modelers, but a consensus seems to be appearing that SASI is not generically suppressed in 3D. Of course, the appearance of SASI needs confirmation also by future 3D simulations that yield successful explosions (none of our 3D models has led to an explosion so far), and numerical simulations might still be different from what happens in real stars. Detecting SASI in the neutrino signal of the next nearby SN would go a long way in testing our hydrodynamical understanding of stellar core collapse. With IceCube and the future Hyper-Kamiokande, a galactic SN offers a realistic opportunity for such a detection at any distance up to 20 kpc, but the signal amplitude strongly depends on the observer direction relative to the main SASI plane of motion.

The main point of our present paper is to provide more details about the neutrino signals of these models and their directional dependence. We stress that observer-related quantities are weighted hemispheric averages with appropriate flux-projection effects as considered here and outlined in our Appendix A. We have also provided, in Appendix B, simple analytic approximation formulas, based on the IBD cross sections of Ref. [107], that allow one to obtain detection rates based on the parameters of an assumed Gamma distribution for the neutrino spectra. In order to translate 3D model output into detection rates, SN modelers would have to provide flavor-dependent luminosities as well as first and second energy moments that are based on such observer-related hemispheric averaging.

In our other companion paper [55] we have reported a new spherical-symmetry breaking effect in the form of LESA. The emission of ν_e and $\bar{\nu}_e$, during the accretion phase, builds up a distinct dipole pattern such that deleptonization happens predominantly in one hemisphere. Therefore, the relative number fluxes of ν_e and $\bar{\nu}_e$ show a strong angular variation. It has not yet been explored what this means in the context of flavor oscillations with neutrino-neutrino refractive effects.

The direction of the LESA dipole and the plane of SASI sloshing and spiral modes are apparently not related—

these are different effects that can coexist. In particular, while we find LESA for all three studied progenitors, SASI occurs only for the heavier ones. Any influence of SASI on the LESA dipole orientation seems to depend on the relative LESA and SASI dipole orientations, both randomly established for each progenitor. LESA survives phases of violent SASI activity, even though it may be somewhat masked by the latter. Further analysis on the LESA phenomenon and hydrodynamical simulations for more SN progenitors are needed to properly disentangle the two effects.

During the standing-shock accretion-powered phase of neutrino emission, several new effects develop in 3D in contrast to the traditional spherically-symmetric picture. This phase offers a rich variety of new hydrodynamical and neutrino-hydrodynamical phenomenology that has only begun to be explored. The theory of neutrino flavor conversion with neutrino-neutrino refraction needs to be further developed to understand its role during this phase. A future high-statistics observation by IceCube and Hyper-Kamiokande will provide opportunities to test such effects, and in particular the appearance of SASI modes.

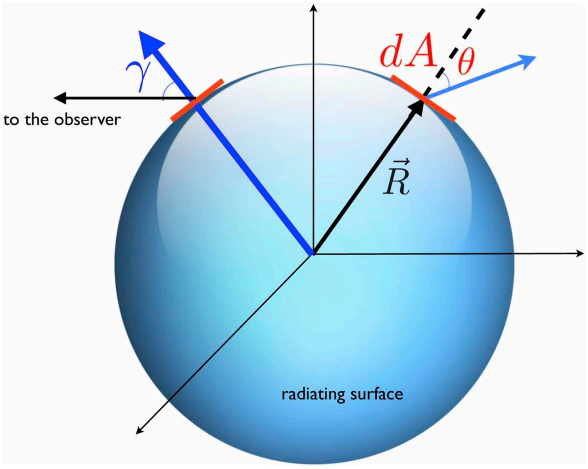

FIG. 17: Sketch of the quantities appearing in the calculation of the SN neutrino flux measured by a distant observer. The neutrino intensity is defined in terms of the location $\mathbf{R}$ of the emitting surface element dA and the angle $\omega = (\theta, \phi)$ of emission relative to the direction $\mathbf{R}$. The observer is located at a distance $D \gg R$ in an arbitrary direction $\Omega = (\Theta, \Phi)$, and γ is the angle between the location of the radiating surface element and the direction of the observer.

Acknowledgements

We thank Ewald Müller for discussions. This research was supported by the Deutsche Forschungsgemeinschaft (DFG) through the Transregional Collaborative Research Center SFB/TR 7 "Gravitational Wave Astronomy" and the Cluster of Excellence EXC 153 "Origin and Structure of the Universe" (http://www.universe-cluster.de), and by the EU through ERC-AdG No. 341157-COCO2CASA. I.T. acknowledges support from the Netherlands Organization for Scientific Research (NWO). Our results could only be achieved with the assistance of high performance computing resources (Tier-0) provided by PRACE on CURIE TN (GENCI@CEA, France) and SuperMUC (GCS@LRZ, Germany) and by the Gauss Centre for Supercomputing (GCS) on SuperMUC. We also thank the Rechenzentrum Garching for computing time on the IBM iDataPlex system *hydra*.

Appendix A: Neutrino Flux Projections

Given the neutrino emission characteristics at the SN from a 3D simulation we need to calculate the flux measurable by a distant observer, closely following Ref. [51]. Given a coordinate system in which the simulation has been performed (see Fig. 17), the observer is located at a large distance $D \gg R$ in an arbitrary direction $\Omega = (\Theta, \Phi)$. Here R is the radius of a sphere near the SN where the neutrino intensities are specified by the output of the code. We have chosen $R = 500$ km so that it is not necessary to apply coordinate transformations and redshift effects between the fluid frame and the distant observer. All quantities depend on time t, which we never show explicitly, and we neglect retardation effects between neutrinos emitted from different regions of the emitting surface.

We assume that the neutrino intensity $I(\boldsymbol{R}, \omega)$ is given in terms of the location $\boldsymbol{R}$ on the emitting surface. The angle $\omega = (\theta, \phi)$ describes the angular emission characteristic relative to the direction $\boldsymbol{R}$ on the surface. While the intensity is usually defined as the local spectral energy density of the neutrino radiation field for a given direction of motion ω times the speed of light, we here take it to be integrated over energy or over a specific energy bin. It is trivial to go back to spectral quantities (differential with regard to neutrino energy).

In order to obtain the energy flux at the location of the observer we have to integrate over solid angles $d\Omega'$ over the surface of the source as seen by the observer and add up the flux contributions emitted by each surface element in the direction of the observer. A given area dA on the emitting surface has the transverse cross section, as seen by the observer, of $\cos\gamma\, dA$ where γ is the angle between $\boldsymbol{R}$ (location of the surface element) and the direction of the observer (see Fig. 17) so that $d\Omega' = \cos\gamma\, dA/D^2$. The observable flux is therefore

$$F_\Omega = \frac{1}{D^2} \int\limits_{\substack{\text{visible}\\ \text{surface}}} dA\, \cos\gamma\, I(\boldsymbol{R}, \omega_\Omega)\,, \qquad \text{(A1)}$$

where ω_Ω is the emission direction toward the observer and F_Ω is the energy flux at distance D in the direction Ω. If the observer interprets this flux as originating from a spherically symmetric source, the measured flux corresponds to the 4π-equivalent luminosity of $4\pi D^2$ times

this expression or

$$L_\Omega = 4\pi \int\limits_{\substack{\text{visible}\\ \text{surface}}} dA\, \cos\gamma\, I(\boldsymbol{R},\omega_\Omega)\,, \tag{A2}$$

where the surface integral is over the part of the surface that is visible to the observer.

Our 3D hydrodynamical simulations are based on the ray-by-ray scheme [64] where in each angular zone one solves a 1D neutrino transport problem so that, within such a zone, the emission is axially symmetric and depends only on the zenith angle, θ, relative to the radial direction. In principle, $I(\boldsymbol{R},\theta)$ can be extracted from the numerical results, but would require a vast amount of post-processing of huge data files. Instead, we fall back on a simple approximation where the directional distribution on each point of the radiating surface can be described by the diffusion approximation for a radial flux [51, 108]

$$I(\boldsymbol{R},\theta) = a\,E(\boldsymbol{R}) + b\,F(\boldsymbol{R})\cos\theta\,, \tag{A3}$$

with E the neutrino energy density and F the neutrino energy flux. In order to determine a and b we refer to the definitions of E and F in terms of angular integrals of the intensity I,

$$E(\boldsymbol{R}) = \frac{2\pi}{c}\int_{-1}^{+1} I(\boldsymbol{R},\theta)\, d\cos\theta \tag{A4}$$

and

$$F(\boldsymbol{R}) = 2\pi\int_{-1}^{+1} I(\boldsymbol{R},\theta)\,\cos\theta\, d\cos\theta\,, \tag{A5}$$

where c is the speed of light. To express both coefficients by the same quantity we assume $F = f\,c\,E$ so that $I(\boldsymbol{R},\theta) = (f^{-1} + 3\cos\theta)\,F(\boldsymbol{R})/4\pi$. The value of f is determined by the requirement that for $F = $ const. on the sphere, after integrating over the entire surface, one obtains the luminosity $L = 4\pi R^2 F$ so that

$$I(\boldsymbol{R},\theta) = \frac{F(\boldsymbol{R})}{2\pi}\left(1 + \frac{3}{2}\cos\theta\right). \tag{A6}$$

Note that since $I \geq 0$, Eq. (A6) is strictly valid only for $\cos\theta \geq -2/3$, which includes inward going radiation for $\cos\theta < 0$. Equation (A6) reproduces the limb-darkening effect—see Ref. [108] for more details. With this result, we finally obtain

$$L_\Omega = 2\int\limits_{\substack{\text{visible}\\ \text{surface}}} dA\,\left(1 + \frac{3}{2}\cos\gamma\right)\cos\gamma\, F(\boldsymbol{R})\,, \tag{A7}$$

where we have inserted $\theta = \gamma$ because the zenith angle of local radiation emission that points in the direction of the observer is identical with γ (see Fig. 17). The value of γ at a surface point $\boldsymbol{R}$ depends, of course, on the observer direction Ω.

In conclusion, the only information from the numerical SN model that we actually use is the radial neutrino-energy dependent flux $F(\boldsymbol{R},\epsilon_\nu)$ on a given surface. From here, we perform projections along the direction of the observer for the energy-dependent fluxes before computing the observable L, $\langle\epsilon_\nu\rangle$, $\langle\epsilon_\nu^2\rangle$ for the neutrino spectral information in the form of an assumed Γ distribution (see Appendix B).

Appendix B: Neutrino Spectra and Inverse Beta Cross Section

The quasi-thermal neutrino spectra produced at the SN can be well approximated in terms of a Gamma distribution which has the normalized form [71, 109],

$$f(\epsilon) = \frac{\epsilon^\alpha}{\Gamma_{\alpha+1}}\left(\frac{\alpha+1}{A}\right)^{\alpha+1}\exp\left[-\frac{(\alpha+1)\,\epsilon}{A}\right], \tag{B1}$$

where Γ is the Gamma function, A an energy scale, and α a shape parameter with $\alpha = 2$ corresponding to a Maxwell-Boltzmann distribution. The spectra are usually "pinched," meaning that usually $\alpha > 2$. For the moments of the distribution we use the notation

$$\epsilon_n = \langle\epsilon^n\rangle = \int_0^\infty d\epsilon\,\epsilon^n\, f(\epsilon)\,. \tag{B2}$$

The first two moments are

$$\epsilon_1 = \langle\epsilon\rangle = A \quad\text{and}\quad \epsilon_2 = \langle\epsilon^2\rangle = \frac{\alpha+2}{\alpha+1}\,A^2\,. \tag{B3}$$

This implies that the shape parameter is given in terms of the first two moments as

$$\alpha = \frac{\epsilon_2 - 2\epsilon_1^2}{\epsilon_1^2 - \epsilon_2} = \frac{\langle\epsilon\rangle^2 - \epsilon_{\rm rms}^2}{\epsilon_{\rm rms}^2}\,. \tag{B4}$$

The rms width of the Gamma distribution is $\epsilon_{\rm rms} = \sqrt{\langle\epsilon^2\rangle - \langle\epsilon\rangle^2} = A/\sqrt{\alpha+1}$. From the numerical data we extract the energy moments ϵ_1 and ϵ_2 and determine A and α accordingly.

The main detection process is inverse beta decay (IBD), $\bar\nu_e p \to n e^+$, where the final-state positron shows up by its Cherenkov radiation. Therefore, the primary $\bar\nu_e$ spectrum must be translated to the corresponding e^+ spectrum. If we take positrons to be massless, ignore the proton-neutron mass difference as well as recoil effects, the cross section is

$$\begin{aligned}\sigma_{\rm naive} &= \frac{G_{\rm F}^2\cos^2\theta_{\rm C}\,(1+3C_A^2)}{\pi}\,\epsilon_\nu^2 \\ &= 9.343\times10^{-44}\ {\rm cm}^2\left(\frac{\epsilon_\nu}{\rm MeV}\right)^2,\end{aligned} \tag{B5}$$

where $G_{\rm F} = 1.166\times10^{-5}\ {\rm GeV}^{-2}$ is the Fermi constant, $\cos\theta_{\rm C} = 0.9746\pm0.0008$ the cosine of the Cabibbo angle, and $C_A = -1.270\pm0.003$ the axial-vector coupling constant. With this simple ϵ_ν^2 scaling, the positron spectrum

would also follow a Gamma distribution with average energy $A_e = A_\nu(3+\alpha_\nu)/(2+\alpha_\nu)$ and $\alpha_e = \alpha_\nu + 2$. An example with $A_\nu = 13$ MeV and $\alpha_\nu = 3$ is shown in Fig. 18 as a thin solid line. The corresponding naive positron distribution has $A_e = \frac{3}{2} A_\nu = 19.5$ MeV and $\alpha_e = 5$, shown as a thin dashed black line.

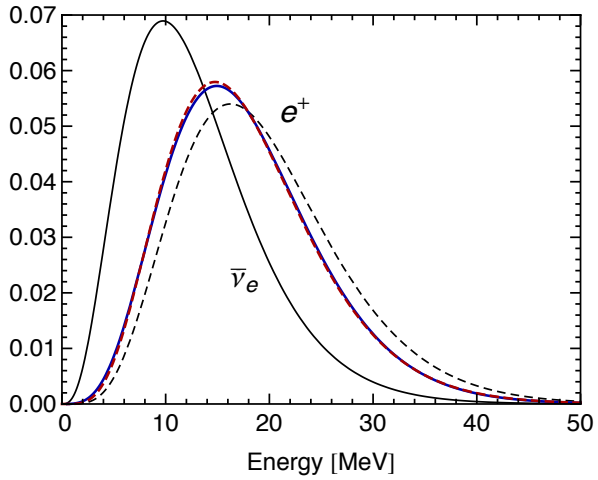

FIG. 18: Normalized energy distribution of $\bar{\nu}_e$, assuming a Gamma distribution (solid black line) with $A_\nu = 13$ MeV and $\alpha_\nu = 3$. Corresponding normalized positron distribution (solid blue line) after folding with inverse-beta decay cross section. Approximation with a Gamma distribution (dashed red line) with same $\langle \epsilon_e \rangle$ and $\langle \epsilon_e^2 \rangle$. Assuming an inverse-beta cross section scaling with ϵ_ν^2 and no recoils gives the dashed black spectrum.

A realistic IBD cross section requires to take into account recoil effects, the neutron-proton mass difference, the positron mass, and nucleon form factors. We use the results of Ref. [107] to derive the positron distribution, shown as a thick blue line in Fig. 18. We compare it with a Gamma distribution (dashed red line) with the same $\langle \epsilon \rangle$ and $\langle \epsilon^2 \rangle$ and find $A_e = 17.86$ MeV and $\alpha_e = 4.76$. We show a normalized spectrum here; the average cross section is approximately 0.74 of the naive result. We conclude that the positron spectrum is also well approximated by a Gamma distribution. (Of course, the positron spectrum strictly begins only at $\epsilon_e = m_e$, but the energy range below a few MeV is irrelevant in practice.)

What remains is to express the positron Gamma-distribution parameters in terms of those of the primary $\bar{\nu}_e$ spectrum. We have derived analytic approximation functions for this transformation. Expressing all energies in MeV, we find

$$A_e = \sqrt{m_e^2 + \left(\frac{3+\alpha_\nu}{1+\alpha_\nu} A_\nu\right)^2} - \frac{5A_\nu}{4(8+\alpha_\nu)} \times \left(\frac{31+9\,\alpha_\nu}{10+7A_\nu} + \frac{170+47\,\alpha_\nu+\alpha_\nu^2}{1+4\alpha_\nu} \frac{A_\nu}{600}\right), \quad \text{(B6)}$$

$$\alpha_e = 2.25 + \frac{0.4}{1+(A_\nu/3.7)^{3.5}} + \frac{1.08\,A_\nu - 0.7}{3+A_\nu}\,\alpha_\nu\,, \quad \text{(B7)}$$

$$\langle \sigma \rangle = 7.37 \times 10^{-46}\ \text{cm}^2\ \frac{2+\alpha_\nu}{1+\alpha_\nu} A_\nu^{2.15} \times \left(\frac{76.64}{\alpha_\nu^{0.021}} - \frac{A_\nu}{\alpha_\nu^{0.24}}\right) \times \left[1 - \exp\left(\frac{-0.25+0.55\,\alpha_\nu}{2.2+\alpha_\nu} - \frac{1+1.6\,\alpha_\nu}{1+4\,\alpha_\nu} A_\nu\right)\right]. \quad \text{(B8)}$$

Typically, these approximation formulas are good to much better than 1% in our range of interest.

[1] K. Scholberg, Ann. Rev. Nucl. Part. Sci. **62**, 81 (2012).
[2] K. Abe *et al.* (Super-Kamiokande Collaboration), Nucl. Instrum. Meth. A **737**, 253 (2014).
[3] T. Mori (for Super-Kamiokande Collaboration), Nucl. Instrum. Meth. A **732**, 316 (2013).
[4] R. Abbasi *et al.* (IceCube Collaboration), Astron. Astrophys. **535**, A109 (2011).
[5] M. Salathe, M. Ribordy and L. Demirors, Astropart. Phys. **35**, 485 (2012).
[6] M. G. Aartsen *et al.* (IceCube Collaboration), arXiv: 1309.7008.
[7] Y.-F. Li, Int. J. Mod. Phys. Conf. Ser. **31**, 1460300 (2014).
[8] K. Abe *et al.* (Hyper-Kamiokande Working Group), arXiv:1109.3262.
[9] S. K. Agarwalla *et al.* (LAGUNA-LBNO Collaboration), JHEP **1405**, 094 (2014).
[10] Long-Baseline Neutrino Experiment Document Database, `http://lbne2-docdb.fnal.gov/`
[11] S. van den Bergh and R. D. McClure, Astrophys. J. **425**, 205 (1994).
[12] W. Li *et al.*, Mon. Not. R. Astron. Soc. **412**, 1473 (2011).
[13] B. C. Reed, Astron. J. **130**, 1652 (2005).
[14] C.-A. Faucher-Giguère and V. M. Kaspi, Astrophys. J. **643**, 332 (2006).
[15] E. F. Keane and M. Kramer, Mon. Not. R. Astron. Soc. **391**, 2009 (2008).
[16] R. Diehl *et al.*, Nature **439**, 45 (2006).
[17] R. G. Strom, Astron. Astrophys. **288**, L1 (1994).
[18] G. A. Tammann, W. Löffler and A. Schröder, Astrophys. J. Suppl. **92**, 487 (1994).
[19] S. M. Adams, C. S. Kochanek, J. F. Beacom, M. R. Vagins and K. Z. Stanek, Astrophys. J. **778**, 164 (2013).
[20] E. N. Alekseev *et al.*, Zh. Eksp. Teor. Fiz. **104**, 2897 (1993) [J. Exp. Theor. Phys. **77**, 339 (1993)].
[21] D. N. Schramm, Comments Nucl. Part. Phys. **17**, 239 (1987).
[22] G. G. Raffelt, Phys. Rept. **198**, 1 (1990).
[23] G. G. Raffelt, Ann. Rev. Nucl. Part. Sci. **49**, 163 (1999).
[24] T. Totani, K. Sato, H. E. Dalhed and J. R. Wilson, Astrophys. J. **496**, 216 (1998).

[25] T. Lund, A. Marek, C. Lunardini, H.-T. Janka and G. G. Raffelt, Phys. Rev. D **82**, 063007 (2010).
[26] T. Lund, A. Wongwathanarat, H.-T. Janka, E. Müller and G. G. Raffelt, Phys. Rev. D **86**, 105031 (2012).
[27] T. D. Brandt, A. Burrows, C. D. Ott and E. Livne, Astrophys. J. **728**, 8 (2011).
[28] I. Tamborra, F. Hanke, B. Müller, H.-T. Janka and G. G. Raffelt, Phys. Rev. Lett. **111**, 121104 (2013).
[29] E. O'Connor, C. D. Ott, Astrophys. J. **762**, 126 (2013).
[30] B. Müller and H.-T. Janka, Astrophys. J. **788**, 82 (2014).
[31] H. A. Bethe and J. R. Wilson, Astrophys. J. **295**, 14 (1985).
[32] H. A. Bethe, Rev. Mod. Phys. **62**, 801 (1990).
[33] H.-T. Janka, Ann. Rev. Nucl. Part. Sci. **62**, 407 (2012).
[34] M. Herant, W. Benz, W. R. Hix, C. L. Fryer and S. A. Colgate, Astrophys. J. **435**, 339 (1994).
[35] A. Burrows, J. Hayes and B. A. Fryxell, Astrophys. J. **450**, 830 (1995).
[36] H.-T. Janka and E. Müller, Astron. Astrophys. **306**, 167 (1996).
[37] A. Marek, H.-T. Janka and E. Müller, Astron. Astrophys. **496**, 475 (2009).
[38] A. Marek and H.-T. Janka, Astrophys. J. **694**, 664 (2009).
[39] B. Müller, H.-T. Janka and A. Marek, Astrophys. J. **756**, 84 (2012).
[40] B. Müller, H.-T. Janka and A. Heger, Astrophys. J. **761**, 72 (2012).
[41] J. W. Murphy and A. Burrows, Astrophys. J. **688**, 1159 (2008).
[42] J. Nordhaus, A. Burrows, A. Almgren and J. Bell, Astrophys. J. **720**, 694 (2010).
[43] C. L. Fryer and M. S. Warren, Astrophys. J. **574**, L65 (2002).
[44] C. L. Fryer and M. S. Warren, Astrophys. J. **601**, 391 (2004).
[45] W. Iwakami, K. Kotake, N. Ohnishi, S. Yamada and K. Sawada, Astrophys. J. **678**, 1207 (2008).
[46] A. Wongwathanarat, H.-T. Janka and E. Müller, Astrophys. J. **725**, L106 (2010).
[47] F. Hanke, A. Marek, B. Müller and H.-T. Janka, Astrophys. J. **755**, 138 (2012).
[48] T. Takiwaki, K. Kotake and Y. Suwa, Astrophys. J. **749**, 98 (2012).
[49] A. Burrows, J. C. Dolence and J. W. Murphy, Astrophys. J. **759**, 5 (2012).
[50] C. D. Ott *et al.*, Astrophys. J. **768**, 115 (2013).
[51] E. Müller, H.-T. Janka and A. Wongwathanarat, Astron. Astrophys. **537**, 63 (2012).
[52] J. M. Blondin, A. Mezzacappa and C. DeMarino, Astrophys. J. **584**, 971 (2003).
[53] L. Scheck, H.-T. Janka, T. Foglizzo and K. Kifonidis, Astron. Astrophys. **477**, 931 (2008).
[54] T. Foglizzo, F. Masset, J. Guilet and G. Durand, Phys. Rev. Lett. **108**, 051103 (2012).
[55] I. Tamborra, F. Hanke, H.-T. Janka, B. Müller, G. G. Raffelt and A. Marek, Astrophys. J. **792**, 96 (2014).
[56] J. W. Murphy, J. C. Dolence and A. Burrows, Astrophys. J. **771**, 52 (2013).
[57] J. C. Dolence, A. Burrows, J. W. Murphy and J. Nordhaus, Astrophys. J. **765**, 110 (2013).
[58] F. Hanke, B. Müller, A. Wongwathanarat, A. Marek and H.-T. Janka, Astrophys. J. **770**, 66 (2013).
[59] S. M. Couch and E. P. O'Connor, Astrophys. J. **785**, 123 (2014).
[60] K. Sumiyoshi, T. Takiwaki, H. Matsufuru and S. Yamada, arXiv:1403.4476.
[61] J. C. Dolence, A. Burrows and W. Zhang, arXiv: 1403.6115.
[62] M. Kachelriess, R. Tomàs, R. Buras, H.-T. Janka, A. Marek and M. Rampp, Phys. Rev. D **71**, 063003 (2005).
[63] P. D. Serpico, S. Chakraborty, T. Fischer, L. Hüdepohl, H.-T. Janka and A. Mirizzi, Phys. Rev. D **85**, 085031 (2012).
[64] M. Rampp and H.-T. Janka, Astron. Astrophys. **396**, 361 (2002).
[65] R. Buras, M. Rampp, H.-T. Janka and K. Kifonidis, Astron. Astrophys. **447**, 1049 (2006).
[66] A. Marek, H. Dimmelmeier, H.-T. Janka, E. Müller and R. Buras, Astron. Astrophys. **445**, 273 (2006).
[67] S. E. Woosley, A. Heger and T. A. Weaver, Rev. Mod. Phys. **74**, 1015 (2002).
[68] S. E. Woosley and A. Heger, Phys. Rep. **442**, 269 (2007).
[69] J. M. Lattimer and F. D. Swesty, Nucl. Phys. A **535**, 331 (1991).
[70] S. W. Bruenn *et al.*, Astrophys. J. **767**, L6 (2013).
[71] M. T. Keil, G. G. Raffelt and H.-T. Janka, Astrophys. J. **590**, 971 (2003).
[72] L. Wolfenstein, Phys. Rev. D **17**, 2369 (1978).
[73] S. P. Mikheev and A. Yu. Smirnov, Yad. Fiz. **42**, 1441 (1985) [Sov. J. Nucl. Phys. **42**, 913 (1985)].
[74] J. Beringer *et al.* (Particle Data Group Collaboration), Phys. Rev. D **86**, 010001 (2012).
[75] A. S. Dighe and A. Yu. Smirnov, Phys. Rev. D **62**, 033007 (2000).
[76] K. Kifonidis, T. Plewa, H.-T. Janka and E. Müller, Astron. Astrophys. **408**, 621 (2003).
[77] K. Kifonidis, T. Plewa, L. Scheck, H.-T. Janka and E. Müeller, Astron. Astrophys. **453**, 661 (2006).
[78] L. Scheck, K. Kifonidis, H.-T. Janka and E. Müeller, Astron. Astrophys. **457**, 963 (2006).
[79] N. J. Hammer, H.-T. Janka and E. Müeller, Astrophys. J. **714**, 1371 (2010).
[80] F. N. Loreti, Y. Z. Qian, G. M. Fuller and A. B. Balantekin, Phys. Rev. D **52**, 6664 (1995).
[81] G. L. Fogli, E. Lisi, A. Mirizzi and D. Montanino, JCAP **0606**, 012 (2006).
[82] A. Friedland and A. Gruzinov, astro-ph/0607244.
[83] J. P. Kneller and C. Volpe, Phys. Rev. D **82** 123004, (2010).
[84] T. Lund and J. P. Kneller, Phys. Rev. D **88**, 2, 023008 (2013).
[85] E. Borriello, S. Chakraborty, H.-T Janka, E. Lisi and A. Mirizzi, arXiv:1310.7488 [astro-ph.SR].
[86] H. Duan, G. M. Fuller and Y.-Z. Qian, Ann. Rev. Nucl. Part. Sci. **60**, 569 (2010).
[87] H. Duan, G. M. Fuller, J. Carlson and Y.-Z. Qian, Phys. Rev. D **74**, 105014 (2006).
[88] G. L. Fogli, E. Lisi, A. Marrone and A. Mirizzi, JCAP **0712**, 010 (2007).
[89] G. G. Raffelt and A. Yu. Smirnov, Phys. Rev. D **76**, 081301 (2007); Erratum *ibid.* **77**, 029903 (2008).
[90] G. L. Fogli, E. Lisi, A. Marrone, A. Mirizzi and I. Tamborra, Phys. Rev. D **78**, 097301 (2008).
[91] B. Dasgupta, A. Dighe, G. G. Raffelt and A. Yu. Smirnov, Phys. Rev. Lett. **103**, 051105

(2009).
[92] G. L. Fogli, E. Lisi, A. Marrone and I. Tamborra, JCAP **0910**, 002 (2009).
[93] B. Dasgupta, A. Mirizzi, I. Tamborra and R. Tomàs, Phys. Rev. D **81**, 093008 (2010).
[94] A. Esteban-Pretel *et al.*, Phys. Rev. D **78**, 085012 (2008).
[95] S. Chakraborty, T. Fischer, A. Mirizzi, N. Saviano and R. Tomàs, Phys. Rev. Lett. **107**, 151101 (2011); Phys. Rev. D **84**, 025002 (2011).
[96] S. Sarikas, G. G. Raffelt, L. Hüdepohl and H.-T. Janka, Phys. Rev. Lett. **108**, 061101 (2012).
[97] N. Saviano, S. Chakraborty, T. Fischer and A. Mirizzi, Phys. Rev. D **85**, 113002 (2012).
[98] J. F. Cherry, J. Carlson, A. Friedland, G. M. Fuller and A. Vlasenko, Phys. Rev. Lett. **108**, 261104 (2012).
[99] S. Sarikas, I. Tamborra, G. Raffelt, L. Hüdepohl and H.-T. Janka, Phys. Rev. D **85**, 113007 (2012).
[100] G. Raffelt, S. Sarikas and D. de Sousa Seixas, Phys. Rev. Lett. **111**, 091101 (2013).
[101] G. Raffelt and D. de Sousa Seixas, Phys. Rev. D **88**, 045031 (2013).
[102] R. S. Hansen and S. Hannestad, Phys. Rev. D **90**, 025009 (2014).
[103] A. Mirizzi, Phys. Rev. D **88**, 073004 (2013).
[104] S. Chakraborty and A. Mirizzi, Phys. Rev. D **90**, 033004 (2014).
[105] S. Chakraborty, A. Mirizzi, N. Saviano and D. de Sousa Seixas, Phys. Rev. D **89**, 093001 (2014).
[106] G. Mangano, A. Mirizzi and N. Saviano, Phys. Rev. D **89**, 073017 (2014).
[107] A. Strumia and F. Vissani, Phys. Lett. B **564**, 42 (2003).
[108] D. Mihalas, *Stellar atmospheres* (W. H. Freeman, San Francisco, 1978).
[109] I. Tamborra, B. Müller, L. Hüdepohl, H.-T. Janka and G. Raffelt, Phys. Rev. D **86**, 125031 (2012).